Article

Magnetocaloric effect of topological excitations in Kitaev magnets

Han Li[1,2], Enze Lv [2], Ning Xi [2], Yuan Gao [2,3], Yang Qi [4], Wei Li [2,3] & Gang Su [1]

Traditional magnetic sub-Kelvin cooling relies on the nearly free local moments in hydrate paramagnetic salts, whose utility is hampered by the dilute magnetic ions and low thermal conductivity. Here we propose to use instead fractional excitations inherent to quantum spin liquids (QSLs) as an alternative, which are sensitive to external fields and can induce a very distinctive magnetocaloric effect. With state-of-the-art tensor-network approach, we compute low-temperature properties of Kitaev honeycomb model. For the ferromagnetic case, strong demagnetization cooling effect is observed due to the nearly free Z_2 vortices via spin fractionalization, described by a paramagnetic equation of state with a renormalized Curie constant. For the anti-ferromagnetic Kitaev case, we uncover an intermediate-field gapless QSL phase with very large spin entropy, possibly due to the emergence of spinon Fermi surface and gauge field. Potential realization of topological excitation magnetocalorics in Kitaev materials is also discussed, which may offer a promising pathway to circumvent existing limitations in the paramagnetic hydrates.

The discovery of magnetocaloric effect (MCE) by Weiss and Piccard in 1917 was a milestone in scientific discovery, bridging the disciplines of magnetics and calorics[1,2]. Under the variation of magnetic fields, there occur a substantial entropy change and thus temperature variations under adiabatic conditions. In particular, sub-Kelvin cooling was achieved through adiabatic demagnetization refrigeration (ADR) with hydrate paramagnetic salts[3,4], which contain nearly free spins that exhibit prominent MCE. However, the paramagnetic coolants also suffer from intrinsic shortcomings, including low magnetic ion density, chemical instability due to the hydrate structure, and low thermal conductivity, etc. Currently, sub-Kelvin ADR plays an important role in space applications[5,6], and also holds great potential for helium-free cooling in advanced quantum technologies[7]. Finding more capable magnetic materials for sub-Kelvin cooling is very demanding for addressing global scarcity of helium supply[8,9].

The low-dimensional quantum magnets have large ion density and stable structure, and may exhibit exotic spin states possessing high entropy density carried by the collective excitations. Cooling through many-body effects, they provide novel magnetocaloric materials and have raised great research interest recently[10–16]. Typically, magnetic entropy gradually releases as spin correlations build up, and it becomes very small when certain spin "solid" order forms at sufficiently low temperature. To avoid such a classical fate, one could resort to highly frustrated magnets with strong spin fluctuations till low temperature. The quantum spin liquids (QSLs)[17–21], resisting any magnetic ordering due to frustration effect and quantum fluctuations, present a particularly promising avenue for exploration[15]. Although QSL systems hold significant potential, there is currently a gap in understanding how the unique properties of QSLs could be harnessed for advanced magnetic cooling.

[1]Kavli Institute for Theoretical Sciences, University of Chinese Academy of Sciences, Beijing 100190, China. [2]Institute of Theoretical Physics, Chinese Academy of Sciences, Beijing 100190, China. [3]Peng Huanwu Collaborative Center for Research and Education, and School of Physics, Beihang University, Beijing 100191, China. [4]State Key Laboratory of Surface Physics and Department of Physics, Fudan University, Shanghai 200433, China. ✉e-mail: w.li@itp.ac.cn; gsu@ucas.ac.cn

In this work, we study the MCE of QSLs in the Kitaev honeycomb system, employing exponential tensor renormalization group approach (Methods)[22–25]. In the ferromagnetic (FM) Kitaev model, we discover a paramagnetic regime with nearly free Z_2 vortices, where the ADR isentropic lines follow a linear scaling with the constant ratio T/B. For the antiferromagnetic (AF) Kitaev case, we uncover a gapless QSL emerging at a remarkably low temperature scale, about 3‰ of the spin coupling strength, which gives rise to an even stronger cooling effect. Such a low temperature scale poses significant challenges for calculations, underscoring the remarkable nature of the gapless QSL. The observed properties, including the specific heat, thermal entropy, spin-lattice relaxation rate, and spin structure factors, strongly suggest the presence of a gapless U(1) QSL with spinon Fermi surface. Our findings establish a robust foundation for the development of magnetic cooling involving Kitaev QSLs and similar systems, which could be examined by conducting magnetocaloric experiments on candidate materials such as $Na_2Co_2TeO_6$.

Results

The Kitaev model and spin fractionalization

We consider the Kitaev honeycomb model under magnetic field B applied along the [111] direction perpendicular to the honeycomb plane,

$$H = K \sum_{\langle i,j \rangle_\gamma} S_i^\gamma S_j^\gamma - B \sum_{i,\gamma} S_i^\gamma, \tag{1}$$

where K is the Kitaev interaction whose absolute value is set as 1 (energy scale), and $\langle i, j \rangle_\gamma$ with $\gamma = \{x, y, z\}$ represents the nearest-neighbor Ising couplings on the γ bond as shown in Fig. 1a.

The Kitaev model has exactly solvable QSL ground states[26,27]. At finite temperature, thermal fractionalization occurs (c.f., Supplementary Note 1), with two types of excitations, namely, the Majorana

fermions and Z_2 gauge fluxes, activated at very different temperature scales T_H and T_L, respectively[28–30]. Consequently, there exists a double-peak specific heat (c.f., the inset of Fig. 1b) and a quasi-plateau with fractional entropy ($\frac{1}{2}\ln 2$, see Fig. 1h) between T_H and T_L. We dub such an intermediate-temperature regime as Kitaev fractional liquid (KFL)[28–31]—a correlated spin state that exhibits spin fractionalization. Intriguingly, although the Kitaev QSL may be fragile upon magnetic fields or other non-Kitaev interactions[32–34], the KFL regime at elevated temperature is robust against these perturbations, different system sizes, and various magnetic fields directions[30,34].

Emergent Curie law and demagnetization cooling

In Fig. 1b, we show the thermal entropy $S_m/\ln 2$ computed under magnetic field B up to $0.8|K|$ for the FM ($K < 0$) Kitaev model. The dashed lines represent the isentropes where the ADR process follows: For initial temperatures $T_i \gtrsim T_H$, the isentropic lines are relatively flat, reflecting a weak field tunability of the correlated spins; however, when the initial temperature is below T_H, the isentropes instead become very steep at small fields. Such a prominent cooling effect is rather unexpected for correlated spin systems, and we ascribe it to the fractional excitations in the peculiar Kitaev systems.

To be specific, at relatively high fields and temperatures, the T-B isentropic lines follow an approximate linear behavior $T \propto B + \text{const.}$ in Fig. 1c, where the constant intercepts in the temperature axis reflect spin interactions in the Kitaev model. Nevertheless, in Fig. 1d, we zoom in into the low-T regime, $T \lesssim 0.1$ and $B \lesssim 0.1$, and find there is a linear scaling $T \propto B$ in isentropes that extrapolate to the origin, representing an emergent Curie-law paramagnetic behavior. The emergent paramagnetism can be further verified by computing the Grüneisen parameter $\Gamma_B \equiv 1/T(\partial T/\partial B)_{S_m}$. At low temperatures, such as $T = 0.05$ ($\beta = 20$), we find a scaling $\Gamma_B \sim 1/B$ as indicated in the inset of Fig. 1e. Moreover, the magnetic susceptibility χ_m is shown in Fig. 1f, from which we find an emergent Curie-law behavior $\chi_m \simeq \frac{C_K}{T+\theta}$ with
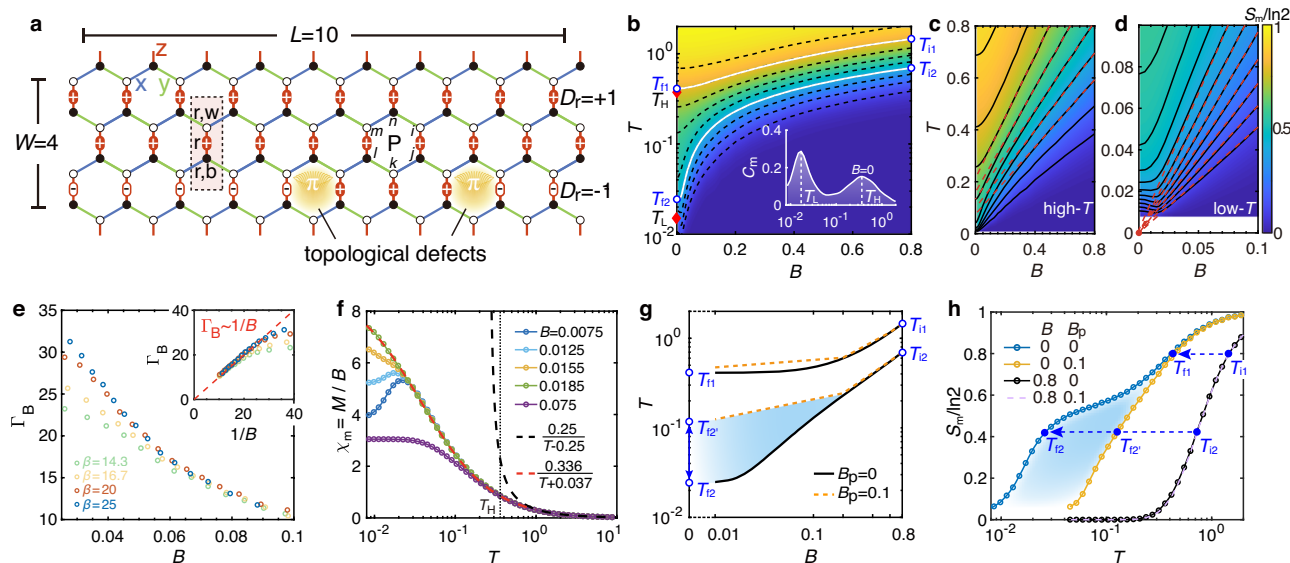

Fig. 1 | Kitaev paramagnetism and demagnetization cooling. a Illustration of the Y-type cylindrical lattice and the topological excitations in the Kitaev model, where blue, green, and red bonds indicate respectively the x-, y-, and z-type interactions. The "+" ("−") sign on the red bonds denote $D_r = +1$ (−1). A pair of π-fluxes (topological defects) can be created by changing the sign of D_r on a vertical bond (or an odd number of bonds). **b** The landscape of isentropes for the FM Kitaev model with field B up to 0.8. At zero field, the specific heat C_m curve shows a double-peak feature at $T_L \simeq 0.017$ and $T_H \simeq 0.36$, as shown in the inset. Two typical, and distinct ADR processes from the initial $T_{i1(2)}$ to the final $T_{f1(2)}$, are indicated with the white lines. **c** High-temperature isentropes following the Curie-Weiss behaviors and **d** low-temperature isentropes intersecting at the origin indicative of the emergent

Curie paramagnetism. **e** The Grüneisen parameter Γ_B at various low temperatures, which follows a $\Gamma_B \sim 1/B$ behavior as shown in the inset. **f** The magnetic susceptibility χ_m at various fields for the FM Kitaev model. The Curie-Weiss fitting at high ($T \gtrsim T_H$) and Curie-law fitting at intermediate temperature ($T_L \lesssim T \lesssim T_H$) are indicated by the black and red dashed curves, respectively. **g** The comparison of the ADR processes with and without the pinning field $B_P = 0.1$, and **h** shows the thermal entropy curves at field $B = 0$ and 0.8. Starting from T_{i2} at $B = 0.8$, the temperature can be decreased to T_{f2} and $T_{f2'}$, in the absence and under a pinning field $B_P = 0.1$, respectively. The former is clearly lower than the latter, as highlighted by the shaded regions in both **g**, **h**. Source data are provided as a Source Data file.

a renormalized Curie constant $C_K \simeq 1/3$ and very small $\theta \simeq 0.037$ in KFL regime[30]. We emphasize that such $1/B$ scaling in Γ_B and Curie-law scaling in χ_m for free spins now appear in the interacting spin system. It suggests the presence of nearly free degrees of freedom that carry significant spin entropies and appear as low-energy excitations in the Kitaev QSL system.

Equation of state in the Kitaev fractional liquid

To understand the paramagnetic behaviors in the KFL regime, we drive the equation of state to describe the gas-like, nearly free Z_2 vortices proliferated at finite temperature ($T > T_L$). To start with, we apply a unitary Jordan-Wigner transformation of the Kitaev Hamiltonian[35],

$$H = \frac{iK_x}{4}\sum_{\langle r',w;r,b\rangle_x}\gamma_{r',w}\gamma_{r,b} - \frac{iK_y}{4}\sum_{\langle r,b;r',w\rangle_y}\gamma_{r,b}\gamma_{r',w} - \frac{iK_z}{4}\sum_r D_r\gamma_{r,b}\gamma_{r,w}, \tag{2}$$

where $\gamma_{r,b(w)}$ represents the bond variable, and $D_r = i\bar{\gamma}_{r,b}\bar{\gamma}_{r,w}$ is related to the gauge flux $W_P = D_r D_{r+1}$ on a hexagon containing vertical bonds r and $r + 1$ (c.f., Fig. 1a), which is a Z_2 variable with values of ± 1. The eigenstates of the Kitaev model can be labeled with these Z_2 variables on each hexagon, and in the ground state, they take the same sign in the same row to ensure the absence of any π flux ($W_P = 1$). Given one D_r flipped, π flux is introduced in two neighboring hexagons that have $W_P = -1$. These π fluxes can be regarded as topological defects, dubbed vision excitations in the Z_2 gauge field, that get activated near the low-temperature scale T_L (c.f., Supplementary Note 1) close to the flux gap[36].

The low-temperature ADR in KFL disappears once the Z_2 fluxes are pinned. In Fig. 1g, we introduce a pinning field coupled to the Z2 fluxes $-B_P\sum_P\sigma_i^x\sigma_j^y\sigma_k^z\sigma_l^x\sigma_m^y\sigma_n^z$ and compare the ADR with and without $B_P = 0.1$, where $\sigma^\gamma = 2S^\gamma$ is the γ-component of the Pauli matrix, and $\{i, j, k, l, m, n\}$ label the six sites in a hexagonal plaquette "P". From $B = 0.8$ and $T_{i2} \simeq 0.8$, the pure Kitaev model undergoes a dramatic temperature decrease to T_{f2} in the ADR process, while the cooling effect is much weaker when the pinning field is applied. This can be understood by checking the entropy curves in Fig. 1h, where the pinning field can freeze the Z_2 flux and move the temperature scale T_L towards a higher temperature. Consequently, the quasi-plateau feature no longer appears under the pinning fields [see the yellow curve in Fig. 1g, h].

As spin flipping in the Kitaev model can create a pair of visions, the latter is thus field tunable and intimately related to the emergent paramagnetism in KFL. A careful analysis (Methods) shows that here the emergent paramagnetic state can be effectively described by the equation of state (EOS)

$$M = C_K B / T,$$

with $C_K \equiv \sum_{j,\gamma}\langle S_{i_0}^\gamma S_j^\gamma\rangle$ computed in the zero-field Kitaev model is the renormalized Curie constant. The EOS indicates that the induced magnetic moment is proportional to the field B and inversely proportional to temperature T, which is the same as that of the ideal Curie paramagnet consisted of free spins. The only difference is the renormalized C_K that originates from the peculiar spin correlations in the Kitaev QSL.

Intermediate-field phase in the AF Kitaev model

Beyond the FM Kitaev model, we find such topological excitation MCE also in the AF Kitaev system. As shown in Fig. 2a, c, the B field applied along [111] direction can give rise to qualitatively different phase diagrams for the FM and AF isotropic Kitaev models[32,37–40]. For the FM

case, we show a magnetic entropy landscape with fields ranging from $B = 0$ to 0.1, where the dip of the isentropes gradually converges to the QCP $B_c \simeq 0.018$[37,39].

For the AF Kitaev model, on the other hand, we find two QCPs at $B_{c1} \simeq 0.2$ and $B_{c2} \simeq 0.36$ with an intermediate phase in between, whose nature is still under active investigations[32,33,37,38,41–43]. In addition to magnetic entropy, the QCPs at B_{c1} and B_{c2} in the AF Kitaev model can also be identified through low-T magnetization curves, matrix product operator entanglements, and spin-structure factors, etc., as shown in Supplementary Notes 2,3.

The magnetic entropy curves vs. temperature are shown in Fig. 2b, d, where we compare the FM Kitaev model (Fig. 2b) with the AF case (Fig. 2d). In the former, we find the fractional entropy remains robust in the KFL regime above the chiral spin liquid (CSL) phase (i.e., above the lower temperature scale T_L). Such a quasi-plateau disappears for large fields, like $B = 0.1$, rendering a large entropy change driven by a relatively small field change. Figure 2d shows the magnetic entropy of the AF Kitaev model as a function of temperature for different magnetic fields. We observe that T_L shifts towards lower temperatures within the CSL phase, with the $\frac{1}{2}\ln 2$ quasi-plateau feature remaining. Moreover, in the intermediate-field regime, e.g., at $B = 0.26$ and 0.3, the release of magnetic entropy is very slow, and T_L becomes no longer observable within the temperature window. As a result, a very prominent MCE occurs for the intermediate phase, which can be made more evident when employing units of measure such as Tesla for magnetic field and Kelvin for temperature (see Supplementary Note 4). The lowest cooling temperature is found below 10 mK, given a proper Kitaev coupling strength, and under a modest magnetic field change. In the following, we exploit various finite-T characterizations to clarify the nature of this intermediate-field phase and to understand the MCE in the AF Kitaev case.

Gapless QSL with possible spinon Fermi surface

In Fig. 3a, we show the results of specific heat C_m and Z_2 flux $\langle W_P\rangle$ for the AF case under out-of-plane fields. By pushing the calculations to an unprecedentedly low-temperature $T/K \simeq 0.001$, we find a low-T scale $T_L^* \simeq 0.003$ indicated in Fig. 3a for the $B = 0.3$ case, which is two orders of magnitude lower than $T_H \simeq 0.3$. Considering the very small values of $\langle W_P\rangle$ in Fig. 3a, we find T_L^* no longer reflects the Z_2 flux gap in the intermediate-field phase, but may be associated with other low-energy excitations.

In Fig. 3b, we present the low-T specific heat and entropy curves, which exhibit a power-law scaling $C_m \sim T^\alpha$ with $\alpha \approx 0.8$ below T_L^*. This finding suggests a gapless nature of the intermediate-field QSL, and the sublinear power-law scaling in qualitative agreement with analytical results suggests the existence of a U(1) spinon Fermi surface[32,33]. The emergence of U(1) gauge field and its coupling to spinons can significantly affect the low-energy properties[44], leading to very soft modes and modified thermodynamic scalings with $\alpha < 1$[45]. The results in Fig. 3b indicate a divergent C_m/T, together with the observation of a specific heat peak at $T_L^* \sim 0.003$, indicating strong spinon-gauge fluctuations. They possibly account for the large spin entropy and explain the prominent MCE observed in Fig. 2c, d.

In Fig. 3c, we show the spin-lattice relaxation rate $S_1(\omega = 0)$ computed via an imaginary-time proxy[46]:

$$S_1(\omega = 0) \equiv \frac{1}{T}\sum_\gamma\sum_{j=1}^N\left[\left\langle S_j^\gamma\left(\frac{\beta}{2}\right)S_j^\gamma(0)\right\rangle - \left\langle S_j^\gamma(\beta)\right\rangle^2\right], \tag{3}$$

which probes the low-energy dynamics. In Fig. 3c, we observe that $S_1(\omega = 0)$ continues to increase even below T_L^* for $B = 0.3$, which indicates the strong spin fluctuations and gapless nature of the intermediate phase. Distinctly, $S_1(\omega = 0)$ decays exponentially as $T^\eta e^{-\Delta/T}$ for $B = 1$ in the gapped (partially) polarized phase.
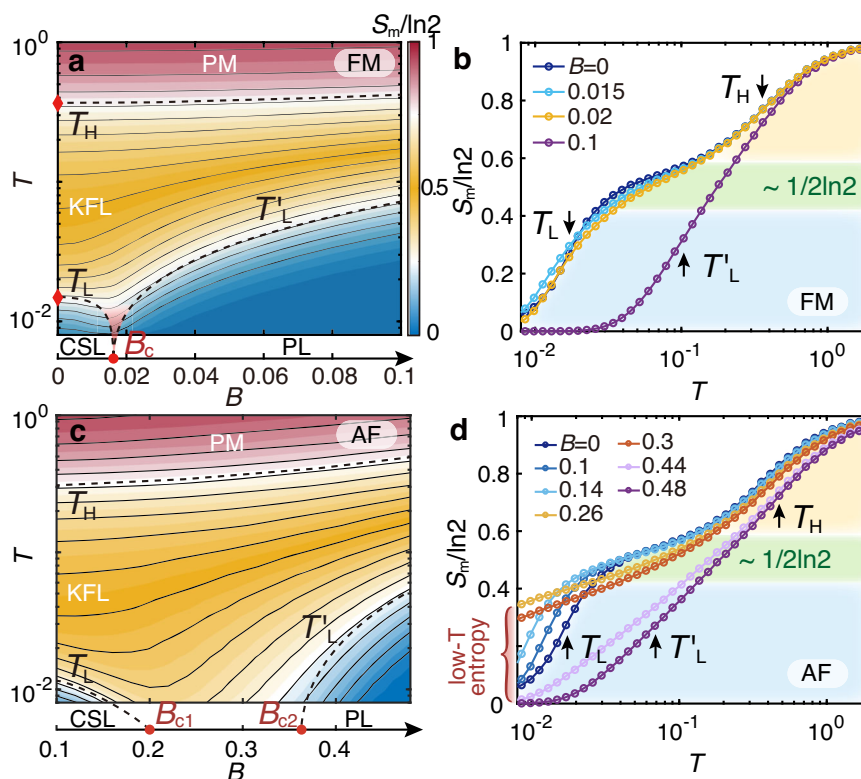
Fig. 2 | The temperature-field phase diagrams and thermal entropy curves.
a, **c** The contour plots of thermal entropies and schematic temperature-field phase diagrams for the FM and AF Kitaev models at finite fields down to $T \simeq 0.008$. There are different regimes in the phase diagram, i.e., the paramagnetic (PM), Kitaev fractional liquid (KFL), chiral spin liquid (CSL), and the polarized (PL) phase. The red dots on the horizontal axis denote the critical fields $B_c \simeq 0.018$[38] for FM and $B_{c1} \simeq 0.2$

and $B_{c2} \simeq 0.36$[33,38] for the AF cases, as obtained with DMRG calculations. The shaded cone emerging from B_c in **a** indicates the quantum critical regime. **b**, **d** The thermal entropy curves at various fields for the FM and AF Kitaev models, where the temperature scales T_H, T_L and T'_L are indicated by the black arrows. Source data are provided as a Source Data file.

To further explore the temperature evolution of the spin states, we show in Fig. 3d the spin structure factors $S(\mathbf{q}) = \sum_{j \in N} e^{i\mathbf{q}(\mathbf{r}_j - \mathbf{r}_{i_0})} (\langle S_{i_0} S_j \rangle - \langle S_{i_0} \rangle \langle S_j \rangle)$, where i_0 represents a central reference site, and the results are obtained by considering all sites and symmetrized over the $\mathbf{q}$ points. When j is restricted within one sublattice of the triangular lattice, we obtain a sublattice spin structure factor as $S_{tr}(\mathbf{q})$. In Fig. 3d, we show the calculated results of $S(\mathbf{q})$ and $S_{tr}(\mathbf{q})$ at various temperatures, where the structure factor peaks move from K_e- to M_e-point in the extended Brillouin zone (BZ) as the system cools down. It is noteworthy that there are still significant changes in the spin structures even at very low temperatures, which converge towards the ground-state results only below T^*_L (c.f., the panels on the right column of Fig. 3d).

Based on the DMRG results of the spin structure factor, a spinon-Fermi-surface U(1) QSL has been proposed, with Fermi pockets around the Γ and M points in the real Brillouin zone[33]. The scattering function is constructed as $\sum_{\mathbf{q}} \delta(\epsilon^S_F(\mathbf{q})) \delta(\epsilon^S_F(\mathbf{q}+\mathbf{k}))$, where $\epsilon^S_F(\mathbf{q}) \equiv \epsilon(\mathbf{q}) - \epsilon_F$ and $\mathbf{k}$ is the momentum transfer across the Fermi surface. Such spinon Fermi surface gives rise to a sublattice spin structure $S_{tr}(\mathbf{q})$ with large intensity at the M points. As shown in the bottom panels in Fig. 3d, $S_{tr}(\mathbf{q})$ develops M-peaks at temperature around T^*_L, reaching a "handshake" with the DMRG calculations.

Overall, our finite-T results support the scenario of a gapless QSL, and the temperature-field phase diagram is shown in Fig. 3e. In the phase diagram, the high-temperature scale T_H determined by the spinon bandwidth is very robust and barely changes at different fields when changing from CSL to gapless U(1) QSL. It is worth noting that the energy scale T^*_L is very small for the emergent gauge field in the intermediate-field phase, which requires high-resolution calculations to resolve its true ground state. This may explain the different

conclusions obtained using various theoretical approaches and approximations, as discussed in previous ground-state studies[32,33,43,47].

Connections to realistic honeycomb-lattice magnets
The Kitaev model can find its materialization in honeycomb-lattice magnets with significant spin-orbit couplings[48]. For example, the 4d- and 5d-electron transition metal based compounds X_2IrO_3 (X = Na, Li, Cu)[49–52] and XR_3 (X = Ru, Yb, Cr; R = Cl, I, Br)[53–63]; the recently proposed 3d-electron Co-based honeycomb magnets[64–70]; the rare-earth chalcohalide REChX (RE = rare earth; Ch = O, S, Se, Te; X = F, Cl, Br, I)[71] and $Ba_9RE_2(SiO_4)_6$ (RE = Ho-Yb)[72]; spin-1 honeycomb-lattice magnet $Na_3Ni_2BiO_6$[73] and spin-3/2 $CrSiTe_3$[74], etc., have been proposed to accommodate Kitaev interactions. Although most of these compounds exhibit long-range magnetic order at sufficiently low temperatures, signatures of Kitaev interaction and spin fractionalization[60,75] have been observed in some of them.

Amongst others, the Co-based Kitaev magnet $Na_2Co_2TeO_6$ has recently attracted great research interest[65,66,76–80]. In Fig. 4a, we calculate the thermal entropy curves based on an effective K-$J_{(1, 2, 3)}$-$\Gamma(')$ model proposed in ref. 79, and compare them to experimental results in Fig. 4b. We note that there are a number of extended Kitaev models[65,77–80] with different parameter sets proposed for $Na_2Co_2TeO_6$, which share some similarities with the K-$J_{(1, 2, 3)}$-$\Gamma(')$ model adopted here. Due to the presence of $J_{(1, 2, 3)}$ and $\Gamma(')$ terms, the ground state has a zigzag AF order (see inset of Fig. 4a) and deviates from a Kitaev QSL, while the magnetic entropy curve shows a shoulder-like feature. This resembles the behavior observed in a pure FM Kitaev model with a pinning field $B_P = 0.1$ shown in Fig. 4a. We also compute the thermal entropy of a K-$J_{(1, 2, 3)}$-$\Gamma(')$ model with reduced J_3 term, where we
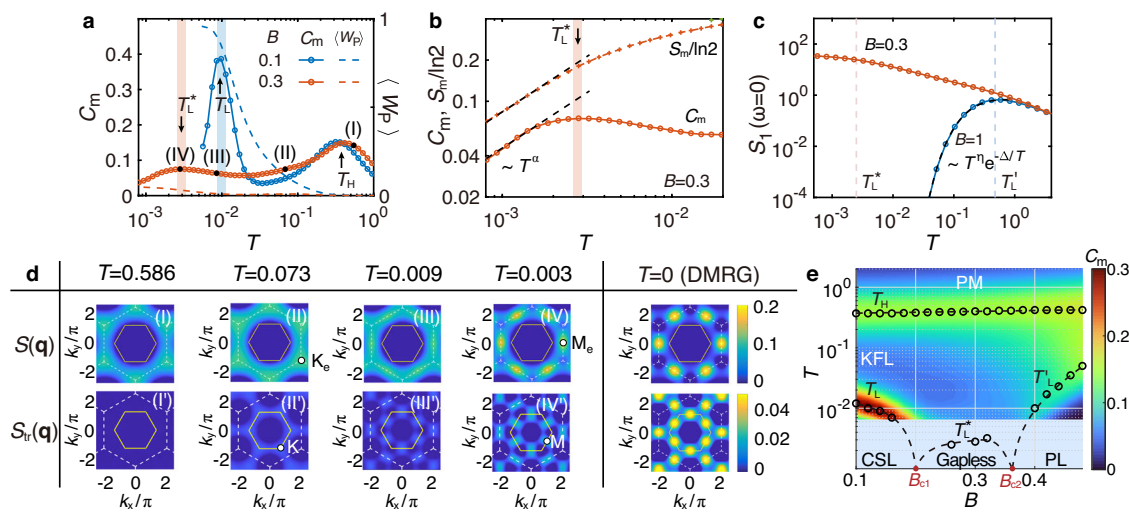
Fig. 3 | The low-temperature calculations on the intermediate-field phase of the AF Kitaev model. a The results of specific heat C_m and expectation $\langle W_P \rangle$ computed on the YC4 × 10 × 2 lattice under two typical fields $B = 0.1$ and 0.3. The calculations are performed down to an extraordinarily low temperature $T/K = 8 \times 10^{-4}$. The temperature scales T_H, T_L, and the remarkably low T_L^* are all indicated by the arrows. **b** The log-log plot of the low-temperature C_m and $S_m/\ln 2$ results under a field of $B = 0.3$, where both curves show power-law scalings T^α ($\alpha \simeq 0.8$) below the low-temperature scale T_L^*. **c** shows the estimate of relaxation rate $S_1(\omega = 0)$ results at $B = 0.3$ and $B = 1$, where in the intermediate-field regime the calculated $S_1(\omega = 0)$ continues to increase even below T_L^*; while in the partially polarized phase it follows $T^\eta e^{-\Delta/T}$ ($\Delta \simeq 0.443$, $\eta \simeq -0.63$) below T_L'. **d** shows the temperature dependence of static spin structure factors $S(\mathbf{q})$ ($B = 0.3$, see the main text) from (I) $T \simeq 0.586$ to (IV) $T \simeq 0.003$ (also marked in panel **a**). The corresponding $S_{tr}(\mathbf{q})$ for one sublattice is shown in the bottom panels (I' to IV'). Representative high-symmetry points K_e, K, M_e, and M in the extended BZ are marked in (II), (II'), (IV), and (IV'), respectively. The ground-state spin structure factor results obtained from DMRG are also displayed in **d**. **e** The contour plot of specific heat C_m down to $T \simeq 0.008$ with $B \in [0.1, 0.48]$. The black circles indicate the peak of the C_m curves, representing the temperature scales T_H, T_L, T_L' and T_L^* separating various magnetic phases, with the dashed line as a guide for the eyes. Source data are provided as a Source Data file.
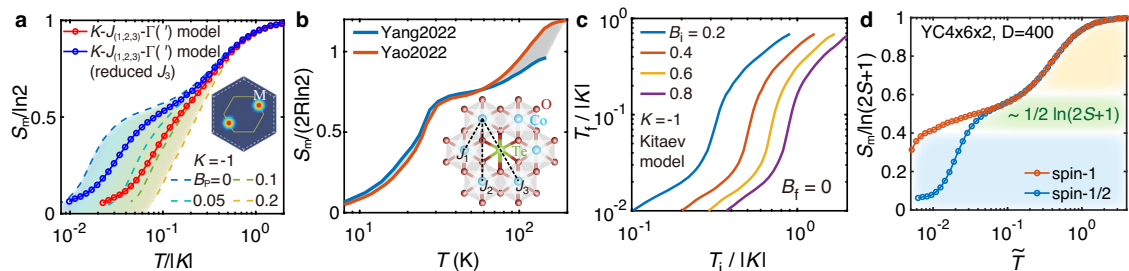

Fig. 4 | Magnetic entropy analysis of Kitaev candidate material $Na_2Co_2TeO_6$ and higher-spin model. a Simulated entropy data based on a realistic K-$J_{(1, 2, 3)}$-$\Gamma(')$ model[79], the parameters (in natural unit) are $K = -1$, $J_1/|K| \simeq -0.03$, $J_2/|K| = 0.007$, $J_3/|K| = 0.17$, $\Gamma/|K| = 0.003$, $\Gamma'/|K| = -0.033$. Although the quasi-plateau feature observed in the pure Kitaev model becomes blurred in the K-$J_{(1, 2, 3)}$-$\Gamma(')$ model (as shown by the red curve), a shoulder-like entropy can be discerned. When the strength of the J_3 is reduced by half, the low-T entropy becomes greatly enhanced. The inset shows the zigzag AF order obtained with the realistic K-$J_{(1, 2, 3)}$-$\Gamma(')$ model[79] in the ground state, and the shaded background with dashed lines represents the FM Kitaev model with various flux pinning fields B_P. **b** The experimental results on $Na_2Co_2TeO_6$ measured by two groups[66,76] with the shaded area highlighting the differences, and a schematic plot of the crystal structure is shown in the inset. **c** The final temperature T_f reached at zero field as a function of the initial temperature T_i under various B_i from 0.2 to 0.8, providing an experimental test of Kitaev fractionalization in future MCE measurements. **d** The entropy curve of spin-1 model compared to the spin-1/2 case, where the fractional entropy plateau is more pronounced and extends to an even lower temperature. The calculations are performed on YC4 × 6 × 2 systems with bond dimension $D = 400$ in panel **d**. The rescaled temperature is $\tilde{T} \equiv T/|K| \cdot \sqrt{(2S+1)/(S(S+1))}$ (see Methods). Source data are provided as a Source Data file.

observe a clearer signature of thermal fractionalization. In Fig. 4b, the experimental data of magnetic entropy are plotted, which exhibit distinct plateau features and suggest a promising cooling capacity. However, there are differences observed between the two experimental curves from different groups[66,76], possibly due to sample dependence, measurement errors, the way to dissociate the phononic and magnetic contributions, or possible electronic excitations beyond the $J_{eff} = 1/2$ manifold.

Given the significant Kitaev interaction present in the effective model considered, the emergence of a shoulder-like feature in our theoretical calculations—a pattern mirrored in experiments on $Na_2Co_2TeO_6$ —suggests that we might be witnessing signatures of fractionalization phenomena, a hallmark of quantum entanglement.

We argue that the non-Kitaev terms in realistic compounds provide an effective "pinning" field B_P, which reduces the low-temperature entropy of topological excitations. Additionally, there are also discrepancies between the simulated curves and the experimental ones, highlighting the urgent need to determine the precise microscopic spin model for $Na_2Co_2TeO_6$.

The results presented in Fig. 4a, b further demonstrate the robustness of spin fractionalization under moderate non-Kitaev interactions. Conversely, these results suggest that the emergence of paramagnetic behaviors could be an indicator of the presence of Kitaev interactions in realistic materials. As shown in Fig. 4c, in practical ADR measurements one can decrease magnetic fields from various initial B_i to final $B_f = 0$ and measure the final cooling temperature

T_f. Besides $Na_2Co_2TeO_6$, its sister material $Na_3Co_2SbO_6$ has also been put forward to host the Kitaev interactions[64]. Moreover, different from these two compounds having strong spin couplings comparable to α-$RuCl_3$[81], we notice there are recent progresses in rare-earth honeycomb-lattice magnet $Ba_9RE_2(SiO_4)_6$ (RE = Ho-Yb)[72] that have moderate couplings suitable for sub-Kelvin cooling. Our studies call for magnetic-specific heat and in particular the MCE measurements on these honeycomb-lattice quantum magnets, which may provides a useful means to probe the Kitaev coupling.

Discussion

To conclude, with the cutting-edge exponential tensor renormalization group approach[23] applied to the Kitaev systems, we construct comprehensive temperature-field phase diagrams for both $K < 0$ and $K > 0$ Kitaev models, where a linear T-B curve in the ADR process is observed in the Kitaev fractional liquid regime. Moreover, for the AF case with $K > 0$, we find thermodynamic evidence for intermediate-field gapless QSL with possible spinon Fermi surface and very pronounced magnetocaloric responses.

With this, we propose that Kitaev magnets hold not only potential applications in topological quantum computing but also in low-temperature refrigeration. Here, beyond the general argument of frustration effects, we establish a concrete connection between QSL physics and MCE through high-precision many-body calculations. The exotic fractional and topological excitations that are highly field-tunable open up new avenues for advanced magnetocalorics.

On the other hand, unlike paramagnetic salts with nearly free local moments, here we reveal a significant cooling effect of the nearly free Z_2 fluxes arising from interacting spins. There are clear advantages of QSL coolants over paramagnetic salts. The ion density of the former can be one order of magnitude greater, and it thus renders a much larger entropy density. Additionally, the hydrate paramagnetic salts suffer from low thermal conductivity and long relaxation time as the spins are diluted and isolated. On the contrary, in Kitaev QSL the spins fractionalize into localized fluxes and itinerant Majorana fermions. The latter exhibits metallic behavior and can enhance thermal conductivity, making the Kitaev magnets truly exceptional candidates as helium-free quantum material coolants. Moreover, such topological cooling also exists in higher-spin Kitaev systems, as shown in Fig. 4d (see also Methods), rendering a scalable cooling capacity with higher spins.

Much like the exploration of low-temperature magnetocalorics on the triangular-lattice quantum antiferromagnet $Na_2BaCo(PO_4)_2$[68,82] has expanded our knowledge of triangular-lattice spin supersolid and its giant cooling effect[16], we expect that the current proposal will lead to future discoveries and advancements in the studies of Kitaev materials. This represents a compelling approach to realize helium-free cooling by tapping into the topological excitations of emergent gauge fields within QSL systems and candidate materials.

Methods

Density matrix and tensor renormalization group approach

The ground state properties are computed by the density matrix renormalization group (DMRG) method, and the finite-temperature properties are computed with the exponential tensor renormalization group (XTRG)[23,24]. As discussed in the main text, the two characteristic temperature scales in the original Kitaev model, i.e., $T_H \simeq 0.36$ and $T_L \simeq 0.017$ are separated by more than one order of magnitude. Therefore, it requires accurate and efficient many-body methods to carry out the low-temperature simulations under zero and finite magnetic fields.

The XTRG method starts from a high-temperature density matrix $\rho_0(\tau_0) = e^{-\tau_0 H}$ with $\tau_0 = 0.0025$, whose matrix product operator (MPO) representation can be obtained accurately up to machine precision[22]. By

multiplying the MPO by itself, the system can be cooled down exponentially fast through $\rho_n \equiv \rho_{n-1} \cdot \rho_{n-1} = \rho(2^n \tau_0)$, and the thermodynamic quantities like free energy, thermal entropy, specific heat, as well as spin correlations, etc, could be calculated with high precision. Such a method has been employed in various 2D spin systems[16,23,24,30,81,83,84], which has been shown to be a highly efficient and powerful tool. In DMRG, we keep up to $D = 1024$ states which leads to a rather small truncation error $\epsilon \lesssim 1 \times 10^{-8}$. In XTRG calculations, with retained bond dimension D up to 600, the truncation errors are about 10^{-3}–10^{-4} down to $T/|K| \simeq 0.001$. It renders well converged results (c.f., Supplementary Note 2). In the simulations, we mainly work with a Y-type cylindrical (YC) lattice YC$W \times L \times 2$ with width $W = 4$ and length $L = 10$, as illustrated in Fig. 1a.

High-spin Kitaev systems

In Fig. 4d we show the entropy curve for the Kitaev model with higher spin $S = 1$, as compared with the $S = 1/2$ case. We find an even more prominent plateau-like structure with about $\frac{1}{2}\ln(2S+1)$ entropy. For the general spin-S Kitaev model, we consider a high-temperature expansion of the partition function up to the second order as $Z(\beta) = (2S+1)^N - \beta Tr[H] + \frac{1}{2}\beta^2 Tr[H^2] + \mathcal{O}(\beta^3)$, where $Tr[H] = 0$ and $Tr[H^2] = \frac{1}{9}K^2 S^2(S+1)^2$. As the high-temperature entropy reads $S_m/N = \ln(2S+1) - \frac{1}{18}K^2 S^2(S+1)^2/T^2$, we can rescale the temperature as $\tilde{T} \equiv T/|K| \cdot \sqrt{(2S+1)}/(S(S+1))$ to collapse the high-temperature entropy curves of different spin-S cases.

The results in Fig. 4d indicate that the spin fractionalization also occurs in higher-spin Kitaev systems, and also huge low-temperature entropies associated with topological excitations. Due to the larger spin quantum number S, there are larger entropies and thus cooling capacity in the spin-1 case than that of the spin-1/2 case. Based on the simulations, we expect the high-S Kitaev materials may serve as excellent refrigerants and also notice that there are recent progresses in Kitaev magnets with higher spin S, including the spin-1 compound $Na_3Ni_2BiO_6$[73] and spin-3/2 $CrSiTe_3$[74].

Derivation of the equation of state in KFL

At zero field, the π-fluxes are virtually non-interacting between the two temperature scales T_L and T_H, giving rise to a paramagnetic behavior described by a concise equation of state. To derive the equation of state for the Kitaev paramagnetism in the intermediate temperature regime, we start with the Hamiltonian

$$H = K \sum_{\langle i,j \rangle_\gamma} S_i^\gamma S_j^\gamma - B \sum_{i,\gamma} S_i^\gamma \equiv H_0 + H', \quad (4)$$

where H_0 and H' are non-commutative, and H' is a perturbation containing three S^γ components coupled to a small field B. We consider the orthonormal basis labeled as $|E^n_{\{W_P\}}\rangle$ as n-th state with the flux configurations $\{W_P\}$, and $|E^{n'}_{\{W'_P\}}\rangle$ represents a n'-th state in the flux-flipped sector $\{W'_P\}$. The operator S_i^γ applied on a site i can flip two adjacent π fluxes with a shared γ bond. Exploiting the Kubo formula, the susceptibility can be expressed as

$$\chi = \sum_{j,\gamma} \int_0^\beta \langle S_{i_0}^\gamma(\tau) S_j^\gamma \rangle_\beta d\tau, \quad (5)$$

where $S_{i_0}^\gamma(\tau) = e^{\tau H} S_{i_0}^\gamma e^{-\tau H}$, and j runs over nearest-neighbor sites of i_0 by γ bond (as well as i_0 itself) in the fractional liquid regime due to the extremely short-range correlations. By inserting the orthonormal basis, we obtain the Lehmann spectral representation

$$\langle S_{i_0}^\gamma(\tau) S_j^\gamma \rangle_\beta = \sum_{\{W_P\},n} \sum_{n'} e^{-\beta E^n_{\{W_P\}}} e^{-\tau \Delta_{n,\{W_P\};n',\{W'_P\}}}$$
$$\langle E^n_{\{W_P\}} | S_{i_0}^\gamma | E^{n'}_{\{W'_P\}} \rangle \langle E^{n'}_{\{W'_P\}} | S_j^\gamma | E^n_{\{W_P\}} \rangle, \quad (6)$$

As the Majorana fermions are only weakly coupled to the Z_2 flux in the intermediate-temperature regime[28], Δ mainly represents the flux excitation gap, i.e., $\Delta_{n,\{W_P\};n',\{W_P'\}} \simeq (E^{n'}_{\{W_P'\}} - E^n_{\{W_P\}}) \sim T_L \ll T \equiv 1/\beta$. Therefore, the decay factor $e^{-\tau\Delta_{n,\{W_P\};n',\{W_P'\}}} \simeq 1$, thus $\langle S^\gamma_{i_0}(\tau)S^\gamma_j\rangle_\beta$ is virtually τ-independent and χ can be expressed as $\chi \simeq \frac{1}{T}\sum_{j,\gamma}\langle S^\gamma_{i_0}S^\gamma_j\rangle_\beta$ in the KFL regime. As $C_K \equiv \sum_{j,\gamma}\langle S^\gamma_{i_0}S^\gamma_j\rangle_\beta$ is nearly a constant below T_H (see Supplementary Note 1), the susceptibility is therefore

$$\chi \approx \frac{C_K}{T}, \tag{7}$$

and the equation of state for KFL is

$$M \approx \frac{C_K B}{T}. \tag{8}$$

Using the Maxwell relation $(\partial M/\partial T)_B = (\partial S_m/\partial B)_T$, we express the magnetic entropy as $S_m = -\frac{C_K B^2}{2T^2} + S_0(T)$. Therefore, $S_{\pi-flux} \approx \frac{1}{2}\ln 2 - \frac{C_K B^2}{2T^2}$ represents the π-flux part in the intermediate-temperature regime, and the isentropes are mainly determined by $S_{\pi-flux}$, which constitute a series of lines through the origin, i.e.,

$$\frac{T}{B} = \text{const.} \tag{9}$$

Data availability
Source data are provided in this paper. The data generated in this study have been deposited in the Zenodo database [https://doi.org/10.5281/zenodo.12736810].

Code availability
All numerical codes in this paper are available upon request to the authors.

References
1. Weiss, P. & Piccard, A. Le phénomène magnétocalorique. *J. Phys.* **7**, 103–109 (1917).
2. Smith, A. Who discovered the magnetocaloric effect? *Eur. Phys. J. H.* **38**, 507–517 (2013).
3. Debye, P. Einige Bemerkungen zur Magnetisierung bei tiefer Temperatur. *Ann. Der Phys.* **386**, 1154–1160 (1926).
4. Giauque, W. F. & MacDougall, D. P. Attainment of temperatures below 1° absolute by demagnetization of $Gd_2 \cdot (SO_4)_3 \cdot 8H_2O$. *Phys. Rev.* **43**, 768–768 (1933).
5. Hagmann, C. & Richards, P. L. Adiabatic demagnetization refrigerators for small laboratory experiments and space astronomy. *Cryogenics* **35**, 303–309 (1995).
6. Shirron, P. J. Applications of the magnetocaloric effect in single-stage, multi-stage and continuous adiabatic demagnetization refrigerators. *Cryogenics* **62**, 130–139 (2014).
7. Jahromi, A. E., Shirron, P. J. & DiPirro, M. J. *Sub-Kelvin Cooling Systems for Quantum Computers*. Tech. Rep. (NASA Goddard Space Flight Center Greenbelt, MD, United States, 2019).
8. Cho, A. Helium-3 shortage could put freeze on low-temperature research. *Science* **326**, 778–779 (2009).
9. Kramer, D. Helium users are at the mercy of suppliers. *Phys. Today* **72**, 26–29 (2019).
10. Zhu, L. J., Garst, M., Rosch, A. & Si, Q. M. Universally diverging grüneisen parameter and the magnetocaloric effect close to quantum critical points. *Phys. Rev. Lett.* **91**, 066404 (2003).
11. Wolf, B. et al. Magnetocaloric effect and magnetic cooling near a field-induced quantum-critical point. *Proc. Natl Acad. Sci. USA* **108**, 6862–6866 (2011).
12. Lang, M. et al. Magnetic cooling through quantum criticality. *J. Phys. Conf. Ser.* **400**, 032043 (2012).
13. Tokiwa, Y. et al. Super-heavy electron material as metallic refrigerant for adiabatic demagnetization cooling. *Sci. Adv.*, **2**, e1600835–e1600835 (2016).
14. Liu, T. et al. Significant inverse magnetocaloric effect induced by quantum criticality. *Phys. Rev. Res.* **3**, 033094 (2021).
15. Liu, Xin-Yang et al. Quantum spin liquid candidate as superior refrigerant in cascade demagnetization cooling. *Commun. Phys.* **5**, 233 (2022).
16. Xiang, J. et al. Giant magnetocaloric effect in spin supersolid candidate $Na_2BaCo(PO_4)_2$. *Nature* **625**, 270–275 (2024).
17. Anderson, P. W. Resonating valence bonds: a new kind of insulator? *Mater. Res. Bull.* **8**, 153–160 (1973).
18. Balents, L. Spin liquids in frustrated magnets. *Nature* **464**, 199–208 (2010).
19. Zhou, Y., Kanoda, K. & Ng, T.-K. Quantum spin liquid states. *Rev. Mod. Phys.* **89**, 025003 (2017).
20. Wen, J., Yu, Shun-Li, Li, S., Yu, W. & Li, Jian-Xin Experimental identification of quantum spin liquids. *npj Quant. Mater.* **4**, 12 (2019).
21. Broholm, C. et al. Quantum spin liquids. *Science* **367**, eaay0668 (2020).
22. Chen, B.-B., Liu, Y.-J., Chen, Z. & Li, W. Series-expansion thermal tensor network approach for quantum lattice models. *Phys. Rev. B* **95**, 161104(R) (2017).
23. Chen, B.-B., Chen, L., Chen, Z., Li, W. & Weichselbaum, A. Exponential thermal tensor network approach for quantum lattice models. *Phys. Rev. X* **8**, 031082 (2018).
24. Li, H. et al. Thermal tensor renormalization group simulations of square-lattice quantum spin models. *Phys. Rev. B* **100**, 045110 (2019).
25. Li, Q. et al. Tangent space approach for thermal tensor network simulations of the 2d hubbard model. *Phys. Rev. Lett.* **130**, 226502 (2023).
26. Kitaev, A. Anyons in an exactly solved model and beyond. *Ann. Phys.* **321**, 2–111 (2006).
27. Hermanns, M., Kimchi, I. & Knolle, J. Physics of the Kitaev model: fractionalization, dynamic correlations, and material connections. *Ann. Rev. Condens. Matter Phys.* **9**, 17–33 (2018).
28. Nasu, J., Udagawa, M. & Motome, Y. Thermal fractionalization of quantum spins in a Kitaev model: Temperature-linear specific heat and coherent transport of majorana fermions. *Phys. Rev. B* **92**, 115122 (2015).
29. Motome, Y. & Nasu, J. Hunting majorana fermions in Kitaev magnets. *J. Phys. Soc. Jpn* **89**, 012002 (2020).
30. Li, H. et al. Universal thermodynamics in the Kitaev fractional liquid. *Phys. Rev. Res.* **2**, 043015 (2020).
31. Yoshitake, J., Nasu, J. & Motome, Y. Fractional spin fluctuations as a precursor of quantum spin liquids: majorana dynamical mean-field study for the Kitaev model. *Phys. Rev. Lett.* **117**, 157203 (2016).
32. Hickey, C. & Trebst, S. Emergence of a field-driven U(1) spin liquid in the Kitaev honeycomb model. *Nat. Commun.* **10**, 530 (2019).
33. Patel, N. D. & Trivedi, N. Magnetic field-induced intermediate quantum spin liquid with a spinon fermi surface. *Proc. Natl Acad. Sci. USA* **116**, 12199–12203 (2019).
34. Yoshitake, J., Nasu, J., Kato, Y. & Motome, Y. Majorana-magnon crossover by a magnetic field in the Kitaev model: continuous-time quantum Monte Carlo study. *Phys. Rev. B* **101**, 100408(R) (2020).
35. Feng, X.-Y., Zhang, G.-M. & Xiang, T. Topological characterization of quantum phase transitions in a spin-1/2 model. *Phys. Rev. Lett.* **98**, 087204 (2007).

36. Panigrahi, A., Coleman, P. & Tsvelik, A. Analytic calculation of the vison gap in the kitaev spin liquid. *Phys. Rev. B* **108**, 045151 (2023).

37. Gohlke, M., Moessner, R. & Pollmann, F. Dynamical and topological properties of the Kitaev model in a [111] magnetic field. *Phys. Rev. B* **98**, 014418 (2018).

38. Zhu, Z., Kimchi, I., Sheng, D. N. & Fu, L. Robust non-Abelian spin liquid and a possible intermediate phase in the antiferromagnetic Kitaev model with magnetic field. *Phys. Rev. B* **97**, 241110 (2018).

39. Jiang, H.-C., Gu, Z.-C., Qi, X.-L. & Trebst, S. Possible proximity of the Mott insulating iridate Na_2IrO_3 to a topological phase: phase diagram of the Heisenberg-Kitaev model in a magnetic field. *Phys. Rev. B* **83**, 245104 (2011).

40. Nasu, J., Kato, Y., Kamiya, Y. & Motome, Y. Successive majorana topological transitions driven by a magnetic field in the Kitaev model. *Phys. Rev. B* **98**, 060416 (2018).

41. Liang, S., Jiang, M.-H., Chen, W., Li, J.-X. & Wang, Q.-H. Intermediate gapless phase and topological phase transition of the Kitaev model in a uniform magnetic field. *Phys. Rev. B* **98**, 054433 (2018).

42. Jiang, H. C., Wang, C. Y., Huang, B. & Lu, Y. M. Field induced quantum spin liquid with spinon Fermi surfaces in the Kitaev model. https://arxiv.org/abs/1809.08247 (2018).

43. Jiang, M.-H. et al. Tuning topological orders by a conical magnetic field in the Kitaev model. *Phys. Rev. Lett.* **125**, 177203 (2020).

44. Shen, Y. et al. Evidence for a spinon Fermi surface in a triangular-lattice quantum-spin-liquid candidate. *Nature* **540**, 559 (2016).

45. Motrunich, O. I. Variational study of triangular lattice spin-1/2 model with ring exchanges and spin liquid state in $\kappa - (ET)_2cu_2(CN)_3$. *Phys. Rev. B* **72**, 045105 (2005).

46. Xi, N. et al. Thermal tensor network approach for spin-lattice relaxation in quantum magnets, http://arxiv.org/abs/2403.11895 (2024).

47. Zhang, S.-S., Halász, G. B. & Batista, C. D. Theory of the Kitaev model in a [111] magnetic field. *Nat. Commun.* **13**, 399 (2022).

48. Jackeli, G. & Khaliullin, G. Mott insulators in the strong spin-orbit coupling limit: From Heisenberg to a quantum compass and Kitaev models. *Phys. Rev. Lett.* **102**, 017205 (2009).

49. Chaloupka, J., Jackeli, G. & Khaliullin, G. Kitaev-Heisenberg model on a honeycomb lattice: Possible exotic phases in iridium oxides A_2IrO_3. *Phys. Rev. Lett.* **105**, 027204 (2010).

50. Singh, Y. et al. Relevance of the Heisenberg-Kitaev model for the honeycomb lattice iridates A_2IrO_3. *Phys. Rev. Lett.* **108**, 127203 (2012).

51. Yamaji, Y., Nomura, Y., Kurita, M., Arita, R. & Imada, M. First-principles study of the honeycomb-lattice iridates Na_2IrO_3 in the presence of strong spin-orbit interaction and electron correlations. *Phys. Rev. Lett.* **113**, 107201 (2014).

52. Choi, Y. S. et al. Exotic low-energy excitations emergent in the random Kitaev magnet Cu_2IrO_3. *Phys. Rev. Lett.* **122**, 167202 (2019).

53. McGuire, M. A., Dixit, H., Cooper, V. R. & Sales, B. C. Coupling of crystal structure and magnetism in the layered, ferromagnetic insulator CrI_3. *Chem. Mater.* **27**, 612–620 (2015).

54. Kim, H.-S., VijayShankar V., Catuneanu, A. & Kee, H.-Y. Kitaev magnetism in honeycomb $RuCl_3$ with intermediate spin-orbit coupling. *Phys. Rev. B* **91**, 241110(R) (2015).

55. Kim, H.-S. & Kee, H.-Y. Crystal structure and magnetism in α-$RuCl_3$: An ab initio study. *Phys. Rev. B* **93**, 155143 (2016).

56. Ran, K. et al. Spin-wave excitations evidencing the Kitaev interaction in single crystalline α-$RuCl_3$. *Phys. Rev. Lett.* **118**, 107203 (2017).

57. Winter, S. M. et al. Breakdown of magnons in a strongly spin-orbital coupled magnet. *Nat. Commun.* **8**, 1152 (2017).

58. Wang, W., Dong, Z.-Y., Yu, S.-L. & Li, J.-X. Theoretical investigation of magnetic dynamics in α-$RuCl_3$. *Phys. Rev. B* **96**, 115103 (2017).

59. Banerjee, A. et al. Proximate Kitaev quantum spin liquid behaviour in a honeycomb magnet. *Nat. Mater.* **15**, 733–740 (2016).

60. Do, S.-H. et al. Majorana fermions in the Kitaev quantum spin system α-$RuCl_3$. *Nat. Phys.* **13**, 1079 (2017).

61. Banerjee, A. et al. Neutron scattering in the proximate quantum spin liquid α-$RuCl_3$. *Science* **356**, 1055–1059 (2017).

62. Imai, Y. et al. Zigzag magnetic order in the Kitaev spin-liquid candidate material $RuBr_3$ with a honeycomb lattice. *Phys. Rev. B* **105**, L041112 (2022).

63. Hao, Y. et al. Field-tuned magnetic structure and phase diagram of the honeycomb magnet $YbCl_3$. *Sci. China Phys. Mech. Astron.* **64**, 237411 (2021).

64. Liu, H., Chaloupka, J. & Khaliullin, G. Kitaev spin liquid in 3d transition metal compounds. *Phys. Rev. Lett.* **125**, 047201 (2020).

65. Lin, G. et al. Field-induced quantum spin disordered state in spin-1/2 honeycomb magnet $Na_2Co_2TeO_6$. *Nat. Commun.* **12**, 5559 (2021).

66. Yao, W., Iida, K., Kamazawa, K. & Li, Y. Excitations in the ordered and paramagnetic states of honeycomb magnet $Na_2Co_2TeO_6$. *Phys. Rev. Lett.* **129**, 147202 (2022).

67. Li, X. et al. Giant magnetic in-plane anisotropy and competing instabilities in $Na_3Co_2SbO_6$. *Phys. Rev. X* **12**, 041024 (2022).

68. Zhong, R., Gao, T., Ong, N.P. & Cava, R. J. Weak-field induced nonmagnetic state in a Co-based honeycomb. *Sci. Adv.* **6**, eaay6953 (2020).

69. Zhang, X. et al. A magnetic continuum in the cobalt-based honeycomb magnet $BaCo_2(AsO_4)_2$. *Nat. Mater.* **22**, 58–63 (2023).

70. Halloran, T. et al. Geometrical frustration versus Kitaev interactions in $BaCo_2(AsO_4)_2$. *Proc. Natl Acad. Sci. USA* **120**, e2215509119 (2023).

71. Ji, J. et al. Rare-earth chalcohalides: a family of van der Waals Layered Kitaev spin liquid candidates. *Chin. Phys. Lett.* **38**, 047502 (2021).

72. Liu, A. et al. $Ba_9RE_2(SiO_4)_6$ (RE = Ho-Yb): a family of rare-earth-based honeycomb-lattice magnets. *Inorg. Chem.* **62**, 13867–13876 (2023).

73. Shangguan, Y. et al. A one-third magnetization plateau phase as evidence for the Kitaev interaction in a honeycomb-lattice antiferromagnet. *Nat. Phys.* **19**, 1883–1889 (2023).

74. Xu, C. et al. Possible Kitaev quantum spin liquid state in 2d materials with $S = 3/2$. *Phys. Rev. Lett.* **124**, 087205 (2020).

75. Banerjee, A. et al. Excitations in the field-induced quantum spin liquid state of α-$RuCl_3$. *npj Quant. Mater.* **3**, 8 (2018).

76. Yang, H. et al. Significant thermal Hall effect in the 3d cobalt Kitaev system $Na_2Co_2TeO_6$. *Phys. Rev. B* **106**, L081116 (2022).

77. Songvilay, M. et al. Kitaev interactions in the co honeycomb antiferromagnets $Na_3Co_2SbO_6$ and $Na_2Co_2TeO_6$. *Phys. Rev. B* **102**, 224429 (2020).

78. Kim, C. et al. Antiferromagnetic Kitaev interaction in $J_{eff} = 1/2$ cobalt honeycomb materials $Na_3Co_2SbO_6$ and $Na_2Co_2TeO_6$. *J. Phys. Condens. Matter* **34**, 045802 (2021).

79. Samarakoon, A. M., Chen, Q., Zhou, H. & Garlea, V. O. Static and dynamic magnetic properties of honeycomb lattice antiferromagnets $Na_2M_2TeO_6$, m = Co and ni. *Phys. Rev. B* **104**, 184415 (2021).

80. Lin, G. et al. Evidence for field induced quantum spin liquid behavior in a spin-1/2 honeycomb magnet. https://doi.org/10.21203/rs.3.rs-2034295/v1 (2022).

81. Li, H. et al. Identification of magnetic interactions and high-field quantum spin liquid in α-$RuCl_3$. *Nat. Commun.* **12**, 4007 (2021).

82. Gao, Y. et al. Spin supersolidity in nearly ideal easy-axis triangular quantum antiferromagnet $Na_2BaCo(PO_4)_2$. *npj Quant. Mater.* **7**, 89 (2022).

83. Li, H. et al. Kosterlitz-Thouless melting of magnetic order in the triangular quantum Ising material $TmMgGaO_4$. *Nat. Commun.* **11**, 1111 (2020).

84. Wang, J. et al. Plaquette singlet transition, magnetic barocaloric effect, and spin supersolidity in the Shastry-Sutherland model. *Phys. Rev. Lett.* **131**, 116702 (2023).

Author contributions

H.L. and W.L. initiated this work. H.L., N.X., and Y.G. performed the tensor-network calculations. H.L., E.L., Y.Q., W.L., and G.S. analyzed the data and conducted theoretical analysis. H.L., G.S., and W.L. prepared the manuscript with input from all authors.

Competing interests

The authors declare no competing interests.

Additional information

Supplementary information The online version contains supplementary material available at https://doi.org/10.1038/s41467-024-51146-7.

Correspondence and requests for materials should be addressed to Wei Li or Gang Su.

Peer review information *Nature Communications* thanks the anonymous reviewers for their contribution to the peer review of this work. A peer review file is available.

Reprints and permissions information is available at http://www.nature.com/reprints

Publisher's note Springer Nature remains neutral with regard to jurisdictional claims in published maps and institutional affiliations.